



Atmospheric Small-Scale Turbulence from Three-Dimensional Hot-film Data

Livia S. Freire¹ · Marcelo Chamecki² · Edward G. Patton³

Received: 1 December 2022 / Accepted: 7 August 2023 / Published online: 7 September 2023
© The Author(s), under exclusive licence to Springer Nature B.V. 2023

Abstract

The behavior of small-scale atmospheric turbulence is investigated using the three-dimensional Canopy Horizontal Array Turbulence Study hot-film data. The analysis relies on an *in situ* calibration versus simultaneous sonic anemometer measurements. The calibration is based on King's law and geometric relationships between the individual hot-film sensors, and is able to account for the errors associated with sensors' misalignment and the high turbulence intensity. The details of the calibration are provided, and its performance is validated by comparing results of spectra and structure functions with standard wind-tunnel data and model spectra. A single 3 h block of data was selected, containing 33 subblocks of 2 min data without error gaps, whose statistics were averaged to provide smooth results. These data were measured above canopy under stable conditions, and correspond to a Taylor Reynolds number $Re_\lambda \approx 1550$. The agreement with wind tunnel results for a similar Re_λ and with model predictions provides a validation for the *in situ* calibration method applied. Furthermore, the results indicate a presence of the bottleneck effect in the lateral and vertical spectra, in addition to a lack of inertial range in the second-order structure function due to the low Reynolds number. An additional analysis of the effect of Reynolds number on the inertial range is provided using atmospheric data from the literature.

Keywords Hot-film · Small-scale turbulence · Sonic anemometer · Spectra · Structure function

1 Introduction

Field measurements correspond to one of the main tools used in the understanding and characterization of atmospheric turbulence. For the wind velocity, the vast majority of these measurements is performed by sonic anemometers, which are robust and resistant instruments developed to function across different weather conditions. Sonic anemometers provide the

✉ Livia S. Freire
liviafreire@usp.br

¹ University of São Paulo, São Carlos, SP, Brazil

² University of California, Los Angeles, CA, USA

³ National Center for Atmospheric Research, Boulder, Colorado, USA

three velocity components, in addition to virtual temperature, by measuring the time taken by sound waves to travel along each of three acoustic paths (Horst and Oncley 2006). These instruments do not require frequent recalibration, but they are limited by the path length between the transducers, which is typically in the order of 0.1 m. As a consequence, turbulent fluctuations with spatial scales smaller than the path length are not captured. In most applications, the scales not captured by the sensor include part of the inertial range and the dissipative scales of the atmospheric flow. Furthermore, the supporting structure of the sensor can also cause flow distortion (Kaimal and Finnigan 1994). Therefore, many turbulence phenomena related to the smallest scales of the flow—including the direct estimation of the turbulent kinetic energy (TKE) dissipation rate itself—cannot be investigated using typical field experiment data.

Differently from field measurements, laboratory experiments of turbulent flows usually rely on hot-film or hot-wire anemometers, also known as constant temperature anemometers (CTA), which are very fine sensors that are able to measure small-scale velocity fluctuations at high frequencies. CTA anemometry is based on the concept of variation of the electrical resistance with temperature, through the use of a heated wire (or film) that senses the changes in heat transfer caused by fluctuations in the fluid velocity. The difference between wire and film is the material composition and diameter (wires are usually one order of magnitude thinner), being recommended for different applications depending on the desired frequency response and resistance (Jørgensen 2005). For atmospheric flows, hot-films are recommended due to their increased strength and stability of calibration, despite the lower frequency response compared to hot-wires (Hasse and Dunckel 1980). CTAs are available in one or multiple sensors per probe, and the output of the sensor is one or multiple time series of voltage that can be directly related to the time series of velocity fluctuations through the use of a calibration curve. One requirement for this method, however, is that the temperature, pressure and composition of the fluid be constant, making the fluid velocity the only variable affecting the heat transfer (Lekakis 1996). Although these conditions can be controlled in the laboratory, they are rarely met in the outdoor environment where atmospheric measurements are performed. The constant calibration required to adjust to changes in air temperature and water vapor mixing ratios make the use of hot-films in atmospheric experiments much less practical.

The most common approach when using hot-film for atmospheric measurements is to perform calibration of each sensor prior to (and sometimes after) the experiment. This can be done in the laboratory or at the experiment site, using a calibration facility or chamber to record the relationship between voltage outputs and known velocities. Laboratory calibration of triple hot-films were used by Miller et al. (1989) in canopy measurements and by Skelly et al. (2002) in the CASES-99 experiment. Calibrations at the experiment site were employed for the 31 single probes in the SLTEST facility of the the Great Salt Lake Desert, USA (Metzger et al. 2007), and by Gulitski et al. (2007) in a flat grassland region near Pardes-Hanna, Israel, where a multi-wire probe was used (20 hot wires plus 5 cold wires for temperature measurements, providing the three velocity components plus temperature, in addition to their spatial and temporal derivatives).

Given the difficulties of frequent and onerous recalibration of the sensor, the idea of calibrating hot-films after the field experiment using the velocity data simultaneously measured by a sonic anemometer has been explored. Known as *in situ* calibration, this approach has been tested by Singha and Sadr (2013) in measurements at the coastal region of Doha, Qatar, using a four-wire anemometer. In the proposed method, the calibration-data reduction is performed at once, and it uses the classical voltage-velocity relationship plus probe geometry information employed in the laboratory calibration in order to match the three sonic velocities

with three hot-film voltages (the fourth validating wire was used in an error minimization function). Similarly, Frehlich et al. (2003) calibrated single hot-wire measurements using simultaneous data of the horizontal velocity from a Pitot tube vaned into the wind.

In a different approach, the calibration-data reduction developed by Kit et al. (2010) and Kit and Liberzon (2016) uses a shallow neural-network that is trained using the hot-film voltage and sonic velocity data measured simultaneously, which is then used as a transfer function to convert the hot-film voltage into a high-frequency velocity time series. The combination of hot-film and sonic anemometer—known as a combo probe—has the additional advantage of automatically adjusting the sensors to the mean wind direction, increasing its ability to provide continuous field measurements without human intervention. The neural-network calibration approach has been validated against traditional calibration using wind tunnel and field data (Kit et al. 2010; Kit and Liberzon 2016). When employed in the Mountain Terrain Atmospheric Modeling and Observations (MATERHORN) field experiment, Kit et al. (2017, 2021) used a combo probe calibrated with a neural network to investigate turbulent bursts and structure functions, respectively, within a 90 min period of stably stratified flow. Recent developments updated the combo probe calibration into a deep learning neural network approach (Goldshmid et al. 2022), eliminating the human-decision-based selection of data for the neural-network training, and improving its automatization.

In this study, we develop a new *in situ* calibration of a triple hot-film probe for the tower data of the CHATS experiment (Patton et al. 2011), with a focus on investigating the small-scale characteristics of the flow. In this particular dataset, the sonic and hot-film sensors were positioned in proximity but pointing in different directions, and turbulence intensity is very often above the acceptable limit of the hot-film probe due to the measurement location's close proximity to the CHATS canopy. We employ the traditional calibration method (voltage-velocity analytical equation plus geometric relationships), as this method allows explicit treatment of aforementioned misalignment of the probes and high turbulence intensity, and provides a direct result. The neural-network method, on the other hand, implicitly combines all features into a single numeric transfer function and may require rescaling of the hot-film velocity obtained. The calibration procedure performed here is similar to the one developed by Singha and Sadr (2013), except that the triple probe provides no additional information for error minimization and the classical voltage-velocity relationship has to be enforced exactly. We evaluate the ability of the triple hot-film in providing reliable information at the small scales by evaluating spectra and structure function ratios, which are very sensitive to measurement and calibration errors (as it will be discussed here) and have theoretical predictions for locally isotropic flows. Additionally, spectral densities and structure functions are also compared to the model spectra of Meyers and Meneveau (2008) and to the wind-tunnel data of Saddoughi and Veeravalli (1994), providing better insights on the quality of the hot-film data and on the characteristics of the small-scale atmospheric flow.

2 Methods

2.1 CHATS Experiment

The Canopy Horizontal Array Turbulence Study (CHATS) is the third of the Horizontal Array Turbulence Study (HATS) experiments, which took place in the spring of 2007 in a deciduous walnut orchard near Dixon, California, USA, with the focus on investigating the main effects of plant canopies on atmospheric turbulence. In the experiment, crosswind arrays and a 30 m

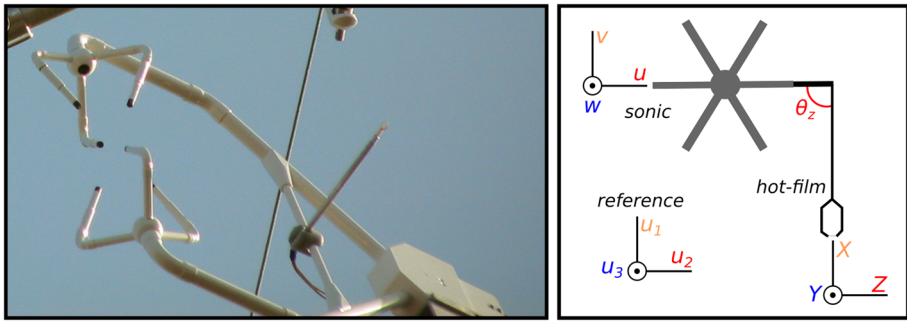


Fig. 1 Left: picture of the sonic and hot-film sensors in the field (hot-film attached to the vertical support of the sonic arms in a 90° angle). Right: top view of the coordinate system of the sonic $\langle u, v, w \rangle$ (pointing westward) and hot-film $\langle X, Y, Z \rangle$ (pointing southward). We define the reference coordinate system as $\langle u_1, u_3, u_2 \rangle$ and redefine the sonic and hot-film data accordingly

profile tower were instrumented with many turbulence, chemistry and meteorological sensors. Among those sensors, there were single hot-film anemometers mounted in the horizontal array and three triple hot-film anemometers mounted in the vertical array (at $z/h = 0.6, 1$ and 1.4 , where $h \approx 10$ m is the mean canopy height), all combined with Campbell Scientific CSAT3 sonic anemometers. In this study, we evaluate the data collected from the triple hot-film at $z/h = 1.4$, which is expected to have lower turbulence intensity (necessary for a better hot-film response) and to present atmospheric surface-layer characteristics with less impact of the canopy flow disturbances. The triple hot-film probe (quartz films covered with a thin nickel film by Dantec Dynamics, model 55R91) was mounted in the vertical support of the sonic arms at an approximately 90° angle relative to the main sonic streamwise direction (Fig. 1). The dataset spans the period between May 13 and June 11 2007 (with-leaves period for the canopy).

Before proceeding with the data analysis, we note that within and above plant canopies, in the roughness sublayer, the flow is strongly impacted by the interaction between the turbulence and the canopy elements. Among other effects, the energy spectrum is altered by the production of eddies in the wake of canopy elements, at the expense of the energy of larger eddies. This process has been termed energy shortcut circuit (see Finnigan 2000) as some of the energy of the large eddies bypass the energy cascade and gets transferred directly into wake-scale eddies. This spectral-shortcut process causes distortions within the inertial range, producing a faster decay at the larger scales and a bump at around the wavenumber corresponding to the wake eddies (Finnigan 2000). This feature is typically observed in one-dimensional spectra measured within the canopy (e.g. Baldocchi and Meyers 1988; Amiro 1990; Cava and Katul 2008), whereas above the canopy one-dimensional spectra present a clear inertial range with characteristics typical of the inertial layer (e.g. Shaw et al. 1974; Su et al. 2004; Mammarella et al. 2008). This inertial range behavior was also observed at CHATS, as discussed by Dupont and Patton (2012, 2022). In particular, the inertial range of the one-dimensional spectra showed very little variation between $z = 14$ m (height of the hot-film used here) and $z = 29$ m (a height which is outside of the roughness sublayer based on the results by Pan and Chamecki, 2016, in particular for the shear-dominated atmospheric stability condition considered here), thereby suggesting that canopy effects on the small scales investigated here are limited to lower heights closer to canopy top (located at $z = 10$ m) and below. It is important to point out, however, that 1D spectra can “smear” features otherwise present in two or three dimensional spectra (Kelly and Wyngaard 2006), and the canopy has

been shown to impact 2D spectra in large-eddy simulation (LES) for z/h up to 2 (Patton et al. 2016). Therefore, the potential impact of the canopy on the results discussed here cannot be ruled out. However, the objective of the present study is to investigate the small-scale structures of the flow, which is reinforced by the similarities with typical inertial-layer 1D spectra present in the literature. Unfortunately, the quality of the hot-film data collected at $z/h = 0.6$ and 1 does not allow for a similar investigation, including the canopy-induced spectral features, due to the frequent violation of acceptable flow direction relative to the fixed probe, and this analysis will be left for future studies.

2.2 Hot-Film Data Processing

The geometry of the triple hot-film probe is such that each of the three films is arranged as the edge of a cube, whose shared vertex points into the streamwise direction. The conversion from the measured voltages of each film (V_j , where $j = 1, 2, 3$ identifies the films) to a velocity vector in the laboratory/field cartesian coordinate system ($u_{h,i}$, where $i = 1, 2, 3$ are the cartesian components) starts with the use of a calibration curve in the form $V_j^2 = a_j + b_j u_{p,j}^{0.45}$ known as King’s law, which provides the velocity vector in the films’ frame of reference ($u_{p,j}$). The second step is the conversion of the velocity vector to the final frame of reference ($i = 1, 2, 3$ for the streamwise, spanwise and vertical directions), through the following matrix multiplications. First, the velocity vector is corrected for yaw and pitch effects using:

$$\begin{pmatrix} u_{p,1}^{*2} \\ u_{p,2}^{*2} \\ u_{p,3}^{*2} \end{pmatrix} = \frac{1}{\alpha} \begin{pmatrix} k^4 - h_p^2 & h_p^4 - k^2 & 1 - h_p^2 k^2 \\ 1 - h_p^2 k^2 & k^4 - h_p^2 & h_p^4 - k^2 \\ h_p^4 - k^2 & 1 - h_p^2 k^2 & k^4 - h_p^2 \end{pmatrix} \begin{pmatrix} u_{p,1}^2 \\ u_{p,2}^2 \\ u_{p,3}^2 \end{pmatrix}, \tag{1}$$

in which $\alpha = h_p^6 - 3h_p^2 k^2 + k^6 + 1$, k and h_p are the yaw and pitch coefficients, respectively, and $u_{p,j}^*$ is the corrected velocity vector in the films’ frame of reference. This relationship, which follows from the Jørgesen’s directional response equation, is general for any hot-film and provides the effective cooling velocity as felt by each film when their yaw and pitch are taken into account (Lekakis et al. 1989).

The second matrix multiplication, which provides the change in frame of reference for the specific geometry of the sensor used here, can be written as:

$$\begin{pmatrix} u_{h,1} \\ u_{h,3} \\ u_{h,2} \end{pmatrix} = \begin{pmatrix} 1/\sqrt{3} & 1/\sqrt{3} & 1/\sqrt{3} \\ -1/\sqrt{2} & 1/\sqrt{2} & 0 \\ 1/\sqrt{6} & 1/\sqrt{6} & -2/\sqrt{6} \end{pmatrix} \begin{pmatrix} u_{p,1}^* \\ u_{p,2}^* \\ u_{p,3}^* \end{pmatrix}. \tag{2}$$

Note that these relationships are presented as provided by the manufacturer (Jørgensen 2005), except for the redefinition of Y or 2 for spanwise and Z or 3 for vertical direction (in the original equations they are reversed). In addition to being different for each wire, the yaw and pitch coefficients may also be a function of mean wind velocity (Lekakis et al. 1989). For better precision, the manufacturer recommends a calibration of these parameters in the lab, as they depend mostly on the geometry of the probe, which may vary from probe to probe but should not change during use (Jørgensen 2005). Since the manufacturer recommended calibration was not performed for this experiment and the probes used were new, we use the manufacturer’s values of $k^2 = 0.04$ and $h_p^2 = 1.2$.

2.3 In-situ Calibration from Sonic Anemometer Data

In this study, sonic anemometer measurements are used to estimate the parameters for the King's law relationship between hot-film voltage and wind velocity for each 30-min period. For practical purposes we define the reference coordinate system as presented in Fig. 1. Note that the reference coordinate system follows the hot-film standard (to use the manufacturer's matrices) but reverses the name between the spanwise and vertical direction, to keep the nomenclature standard in the atmospheric community (i.e., u_1, u_3, u_2 corresponding to streamwise, vertical and spanwise directions). The measurement frequencies are 60 Hz and 2 kHz for sonic and hot-film, respectively. The first step for calibration is to obtain the effective cooling velocity of each film ($u_{p,j}$) from the sonic raw data ($u_{s,j}$). This is done by converting the sonic velocity to the films' frame of reference and accounting for the yaw and pitch effects, using the inverse matrices of the transformations (1) and (2), i.e.,

$$\begin{pmatrix} u_{p,1}^* \\ u_{p,2}^* \\ u_{p,3}^* \end{pmatrix} = \frac{1}{6} \begin{pmatrix} 2\sqrt{3} & -3\sqrt{2} & \sqrt{6} \\ 2\sqrt{3} & 3\sqrt{2} & \sqrt{6} \\ 2\sqrt{3} & 0 & -2/\sqrt{6} \end{pmatrix} \begin{pmatrix} u_{s,1} \\ u_{s,3} \\ u_{s,2} \end{pmatrix}, \quad (3)$$

and:

$$\begin{pmatrix} u_{p,1}^2 \\ u_{p,2}^2 \\ u_{p,3}^2 \end{pmatrix} = \begin{pmatrix} k^2 & 1 & h_p^2 \\ h_p^2 & k^2 & 1 \\ 1 & h_p^2 & k^2 \end{pmatrix} \begin{pmatrix} u_{p,1}^{*2} \\ u_{p,2}^{*2} \\ u_{p,3}^{*2} \end{pmatrix}. \quad (4)$$

Now, the vector $u_{p,j}$ comes from the sonic anemometer, and it can be compared to the voltage measured simultaneously by the hot-film. Note that due to the fact that the sensors are not collocated (Fig. 1), in addition to the path-averaging and other mechanical effects in the sonic anemometer, the higher frequencies of both signals can differ significantly. Therefore, in order to apply the King's law for each 30 min block, the two signals (sonic velocity and hot-film voltage) are low-pass filtered with a spectral cut-off filter at frequency of 0.05 Hz (a conservative choice). Based on the sonic's path-averaging alone, the cut-off frequency should be at most $0.1\bar{u}_1/(2\pi p_l)$ (Horst and Oncley 2006), where $p_l = 0.115$ m is the path length of the CSAT3. Therefore, the selected cut-off frequency will not violate the path-averaging requirement as long as $\bar{u}_1 > 0.003$ m s⁻¹. Note also that the velocity values available for calibration are dominated by the lower frequencies. After the obtention of the parameters a_j and b_j , the procedure described in Sect. 2.2 can be applied and hot-film velocity time series are obtained. Except for calibration, all other results presented here use the original data for both sensors (not low-pass filtered).

2.4 Initial Data Selection

In hot-film measurements, when the velocity vector falls outside the first octant of the $u_{p,j}$ space (where all three velocity components are positive), a problem known as rectification occurs, due to the inability of the hot-film to distinguish the direction of the velocity vector (Maciejewski and Moffat 1994). Furthermore, in Eq. (1), the square of the corrected velocity $u_{p,j}^*$ is related to the square of the effective cooling velocity $u_{p,j}$, disregarding directional information. In this relationship, a square-root of a negative term can occur when one of the three velocity components of $u_{p,j}$ is sufficiently different from the other two. If the three films always point into the streamwise direction, the three velocity components $u_{p,j}$ should be of similar magnitude. However, due to fluctuations in wind direction and intensity, it is

very common to have a square root of a negative number, creating gaps in the time series. Therefore, by using this calibration approach, the presence of gaps guarantee that no data contamination caused by the incorrect wind direction is present in the final dataset.

Fortunately, this is not an issue in the calibration step, since in the conversion of sonic data into the films' frame of reference there is no mechanism to produce a negative radicand (Eq. 4). Furthermore, the low-pass filtering of the calibration step significantly reduces these fluctuations. For that reason, the calibration step is performed for each 30 min block. However, the final hot-film time series is generated as smaller subblocks of data between the gaps (see Fig. 12 in the Appendix). Note that we cannot perform calibration for small subblocks of data (potentially excluding the gaps) because the calibration step relies on the low-frequency similarity between the two sensors. The final subblocks of data also do not present rectification issues, as observed *a posteriori*.

Because the hot-film probe needs to be pointed into the streamwise wind direction, we started by selecting 30 min blocks of data whose mean wind direction is within a 10° cone from the hot-film streamwise direction. By setting the minimum size of the subblock to 30 s, we further select blocks that have a minimum of 25 subblocks, in order to obtain turbulence statistics with reduced scatter from the average across subblocks (see illustration in the Appendix).

Finally, we note that, by using this calibration approach, we were able to observe that the calibration is very sensitive to errors in the alignment between the hot-film probe and the sonic anemometer. From the experimental setup, we noticed that there is a 180° rotation about the hot-film X -axis (i.e., the probe was mounted "upside-down"), which is taken into account when processing the raw data by multiplying the vector by a rotation matrix. We do not expect any rotation about the spanwise axis of the hot-film due to the type of mounting support used (see Fig. 1), but a small rotation about the vertical axis is possible. During the experiment, the hot-film and sonic anemometers were deployed with an estimated 90° rotation about the vertical axis between them (measured by hand with a magnetic compass). Assuming that this 90° rotation about the vertical axis is accurate, we observe that velocity derivative variances from the blocks selected using the criteria defined above all exhibit a bias from the expected behavior for isotropic flows $((\partial u_i / \partial x_1)^2 / (\partial u_1 / \partial x_1)^2 = 2, i = 2, 3)$, estimated using Taylor's frozen turbulence hypothesis after subtraction of the mean velocity). As mentioned by Gulitski et al. (2007), large deviations from local isotropy in the context of hot-film measurements in the atmospheric boundary layer are likely an indication of calibration error rather than a real physical phenomenon. For this reason, we tested the impact of taking into account a small rotation error about the vertical axis of the hot-film (θ_z in Fig. 1), and the result showed a clear trend of the ratios as a function of θ_z (Fig. 2). This is in accordance with the assumption of cross-contamination between the velocity components due to misalignment between sensors. The trend indicates that the most likely correct position corresponds to $\theta_z = 85^\circ$, when the isotropy ratios are similar to each other (although biased toward ~ 2.2 , possibly due to the anisotropy in the spectral bump, see discussion in Sect. 4.1). We adopt this angle (instead of the originally reported 90° angle) during hot-film calibration also using a rotation matrix. This is an example of how sensitive the results can be to small experimental errors.

2.5 Final Data Selection

Very few 30 min blocks of data satisfied the stringent wind angle requirements for the hot-film probe calibration to be reliable during most of the block (i.e. within $\pm 10^\circ$ of θ_z). For that reason, no additional quality-control test needed to be performed in the data.

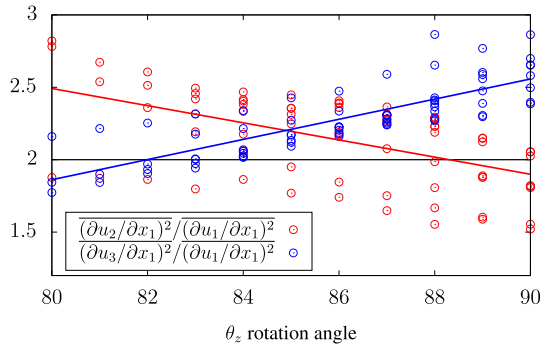


Fig. 2 Ratios of the velocity derivative variances $\overline{(\partial u_2/\partial x_1)^2}/\overline{(\partial u_1/\partial x_1)^2}$ in red, $\overline{(\partial u_3/\partial x_1)^2}/\overline{(\partial u_1/\partial x_1)^2}$ in blue) as a function of the rotation angle about the hot-film vertical axis (θ_z). Horizontal black line corresponds to the theoretical value of 2, and red and blue lines correspond to the linear fit of each ratio as a function of θ_z . Each pair of circles correspond to the result for a different 30 min block that passed the selection criteria

Most blocks satisfying the criteria occurred in the early hours of June 10, spanning a continuous period of 3 h. Due to their similar flow conditions (see Appendix), and in order to increase the subblock size and reduce data scatter, we combined them into a single 3 h block from 03:30 h to 06:30 h local time. Table 1 provides the flow statistics for this block, which has a mean wind of 2.21 m s^{-1} in a 5.94° angle, and corresponds to weakly stable condition (stability parameter $(z - d_o)/L_o = 0.29$, where d_o is the canopy displacement height and L_o is the Obukhov length, see Table 1 for details). The turbulence intensity, defined as $k^{1/2}/\bar{u}_1$, is equal to 0.22, which is above the 0.15 limit of the probe (Jørgensen 2005) and explains the large number of error gaps. A single calibration is performed for the entire 3 hour period (see Fig. 3). Notice the agreement in the low-frequencies between the compensated hot-film voltage and sonic velocity spectra rotated into the films' frame of reference. The deviations in the high-frequency range result from limitations of the sonic anemometer in this frequency range (path-averaging and aliasing, for example), and start around 0.3 Hz, as expected for the path-averaging attenuation $(0.1\bar{u}_1/(2\pi p_l)) = 0.31 \text{ Hz}$, Horst and Oncley (2006)). We note that reproducing all statistics presented here using a cut-off frequency of 0.3 Hz (instead of the chosen 0.05 Hz) generates no relevant differences in our results or conclusions (not shown). As these spectra are in the hot-films's frame of reference, they are dominated by the streamwise velocity component. The presence of an inertial range is already clear in the hot-film data, and the limitation of the corresponding sonic data is also already visible. In interpreting sonic data presented here, it is important to bear in mind that the 85° arrangement is likely impacting the quality of the sonic result, as it will be discussed in the Sec. 4. Furthermore, we have decided not to use the transducer shadowing correction proposed by Horst et al. (2015), because the attenuation for the variances is small and very similar for all three components for a wind direction close to 90 degrees. In addition, the effect of the correction on the CSAT3 sonic anemometer spectra has been shown to generate only a small improvement on the inertial range isotropy ratios, even for small wind directions (Peña et al. 2019).

From this calibration, 33 subblocks of 2 min data were obtained, which were averaged to provide the results presented next. Because a 2 min sample size can be small compared to the integral time scale, tapering the time series is recommended to compensate for the sample size effect on the spectra (Kaimal and Finnigan 1994). However, when comparing the 2 min sonic spectra to the original 3 h spectra, the spectral loss was negligible for the analyses

Table 1 Flow parameters for the selected block (06/10/2007 03:30 h–06:30 h): $(z - d_o)/L_o$ is the Obukhov stability parameter, in which $z = 14$ m is the measurement height, $d_o \approx 0.75h = 7.5$ m is the canopy displacement height (estimated for this canopy under near-neutral conditions by Shapkaliyevski et al. (2016)), $h \approx 10$ m is the canopy height and $L_o = 22.7$ m is the Obukhov length. The mean wind velocity \bar{u}_1 , friction velocity u_* , turbulent kinetic energy k , turbulence intensity $TI = k^{1/2}/\bar{u}_1$, velocity standard deviation σ_i and heat flux $\overline{w'\theta'}$ were measured at 1.4h. Primes indicate fluctuations from the block average (overbar). The mean wind direction is relative to the reference u_1 direction (hot-film axis). a_j, b_j are the King’s law parameters for film j . ε from the integral of the dissipation spectrum (average of the three components, Eq. 5), $\nu = 15.16 \times 10^{-6} \text{ m}^2 \text{ s}^{-1}$, $\eta = (\nu^3/\varepsilon)^{1/4}$, $\lambda = u'(15\nu/\varepsilon)^{1/2}$, $Re_L = k^2/(\varepsilon\nu)$, $Re_\lambda = u'\lambda/\nu = (20Re_L/3)^{1/2}$, where $k = (\overline{u_1^2} + \overline{u_2^2} + \overline{u_3^2})/2$ is the turbulent kinetic energy and $u' = (2k/3)^{1/2}$ is the Taylor velocity scale (Pope 2000)

Statistics of the entire 3h-block	
z/h	1.4
\bar{u}_1 (m s ⁻¹)	2.21
mean wind direction (°)	5.94
u_* (m s ⁻¹)	0.21
k (m ² s ⁻²)	0.23
TI	0.22
$\overline{w'\theta'}$ (K m s ⁻¹)	-0.03
$(z - d_o)/L_o$	0.29
Calibration	
a_1, b_1	1.35, 2.23
a_2, b_2	1.24, 2.24
a_3, b_3	1.35, 2.25
Statistics of the average of the 33 2-min subblock	
$\sigma_1, \sigma_2, \sigma_3$ (m s ⁻¹)	0.37, 0.34, 0.28
ε (m ² s ⁻³)	4.88×10^{-3}
η (mm)	0.919
λ (cm)	7.12
Re_λ	1550
Re_L	3.6×10^5

performed here, and tapering the time-series using a Hamming window (as suggested by Kaimal and Finnigan (1994)) had virtually no effect (not shown). Therefore, tapering was also not included in the final analyses.

A sample of the final velocity time series from the hot-film and sonic data is presented in Fig. 4. Although some discrepancies can be observed in certain data intervals, the large-scale fluctuations are very similar between the two sensors. As expected, clear differences in the small scales are easily identified when the time series are displayed in details (inset of Fig. 4). A comparison of the two filtered time series is provided in the Appendix.

Table 1 also provides some statistics from the average of the 33 2 min subblocks, including the flow variances and Kolmogorov and Taylor length scales. The selected data correspond to a Taylor Reynolds number $Re_\lambda = 1550$. The mean dissipation rate was estimated from the average of the values obtained from the numerical integral of each dissipation spectrum, i.e.,

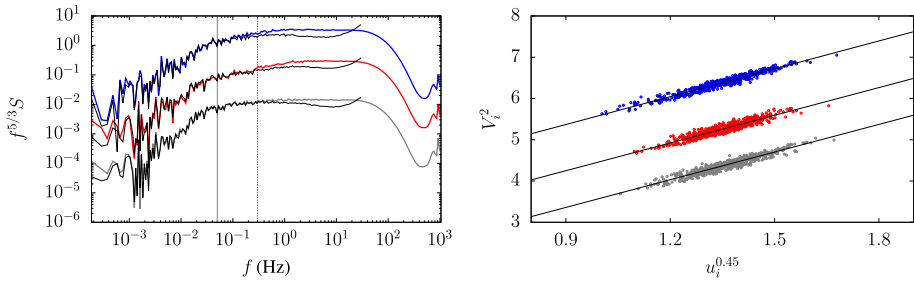


Fig. 3 **a** Hot-film voltage (color lines) and sonic velocity (black lines) compensated spectra in the hot-film frame of reference (all three components in $\approx 35^\circ$ angle with the streamwise direction); **b** King’s law calibration curve (dots are data, line is the best linear fit), for each film (1-grey, 2-red, 3-blue, 2 and 3 are vertically shifted). Spectra were smoothed using bin averages in log scale. The match between voltage and velocity spectra is obtained by vertically shifting the voltage spectra manually, in order to show that they behave similarly (absolute values are not relevant). Vertical lines corresponds to the low-pass filter cut-off frequency used to select the calibration curve data (0.05 Hz, solid black line) and the cut-off frequency limitation from the sonic path-averaging (0.3 Hz, dashed blue line)

$$\varepsilon = \frac{1}{3} \left\{ 15\nu \int_{k_{1,0}}^{k_{1,\infty}} k_1^2 E_{11}(k_1) dk_1 + \frac{15}{2} \nu \int_{k_{1,0}}^{k_{1,\infty}} k_1^2 E_{22}(k_1) dk_1 + \frac{15}{2} \nu \int_{k_{1,0}}^{k_{1,\infty}} k_1^2 E_{33}(k_1) dk_1 \right\}, \tag{5}$$

in which $[k_{1,0}, k_{1,\infty}]$ is the streamwise wavenumber interval with available data. Taylor’s frozen turbulence hypothesis was used to convert frequency into wavenumber.

Regarding the use of the Taylor’s frozen turbulence hypothesis in high-frequency turbulence measurements, it is important to take into account the possible errors caused by the fluctuating advection velocity, as evaluated for example by Wyngaard and Clifford (1977). The corrections proposed by Wyngaard and Clifford (1977) correspond to constant factors applied to the velocity derivative variances and spectra, which are a function of the turbulence intensity and were estimated assuming Kolmogorov’s inertial range model for the spectrum. The respective correction factors for $(\partial u_i / \partial x_1)^2$ estimated for this dataset are 0.911, 0.952, 0.948 for $i = 1, 2, 3$, respectively. These corrections would reduce the value of ε by 7%. The correction factors for $E_{\alpha\alpha}$ are 0.979, 0.996, 0.994 for $\alpha = 1, 2, 3$ respectively, which has a negligible effect on isotropy ratios. Because these corrections are within the variability of the 33 subblocks and they do not impact any analysis or conclusion of this study, we chose to not include the corrections. Finally, we note that the sensor’s length of $l_h = 1.25 \text{ mm} = 1.36\eta$ is not expected to introduce attenuation at the dissipation scales for these data.

3 Reference Data

3.1 Saddoughi and Veeravalli (1994)

Turbulence measurements from a wind-tunnel experiment with Re_λ up to 1500 were obtained in the Full-Scale Aerodynamics Facility at NASA Ames Research Center, in which a boundary layer developed over a rough surface. The dataset resulting from this experiment has been a reference for boundary-layer flows since its publication (Pope 2000), as it pro-

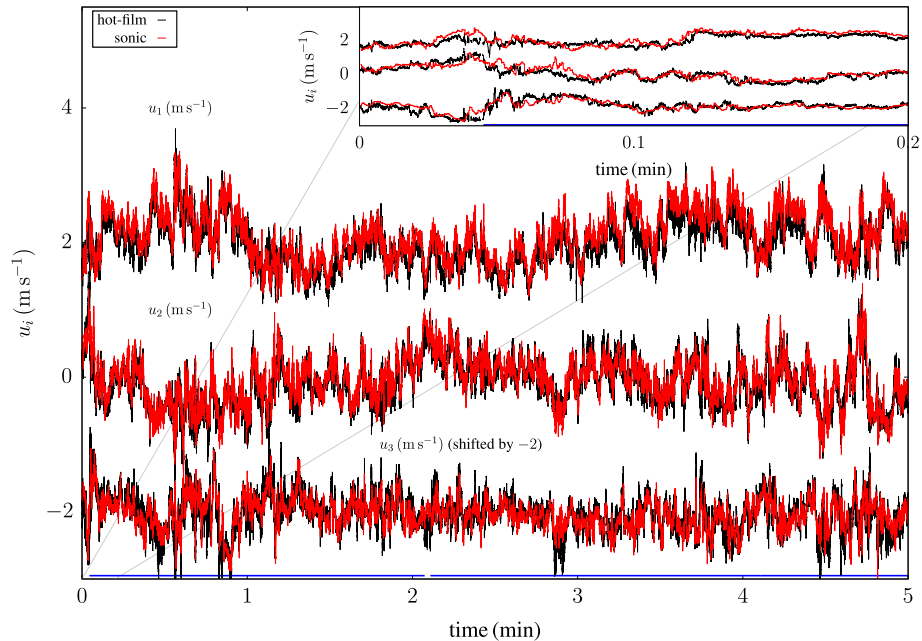


Fig. 4 Sample of velocity time series from sonic (red) and hot-film (black) anemometers, starting at June 10 03:30h local time. Inset is a closer look into the first 12 s. Blue lines at the bottom indicate the 2-min subblocks without data gaps for this sample

vided at the time the highest Reynolds number ever attained in a wind-tunnel. These results comprised spectra and second- and third-order structure functions, including their ratios, providing evidence of a locally isotropic flow, with exponential decay at the dissipation range and the presence of spectral bumps at the transition between the inertial and dissipation scales.

In this study we selected the $Re_\lambda = 1450$ data as a reference, due to the similar Re_λ value compared to the CHATS data. The selected dataset corresponds to their mid-layer high-speed case (the distance from the ground is 400mm, note that Saddoughi and Veeravalli (1994) use y to represent vertical distance). The value of $\varepsilon = 49 \pm 10\% m^2 s^{-3}$ was estimated using the Kolmogorov’s law for the inertial range with $C_k = 1.5$, as a direct estimate was not possible for that specific case. The value of $C_k = 1.5$ was derived based on the compensated spectra of the mid-layer low-speed case ($Re_\lambda \approx 600$), which had $\varepsilon = 0.33 \pm 10\% m^2 s^{-3}$ estimated from the integral of the dissipation spectra. These values were used to nondimensionalize their compensated spectra. Using their third-order structure functions, the values of ε were estimated as about 20% lower for both low and high-speed cases ($\varepsilon = 0.26$ and $40 m^2 s^{-3}$, corresponding to $Re_\lambda = 670$ and 1500, respectively), which they used to nondimensionalize their second and third-order structure functions. In here, we used this estimate from the third-order structure function to plot all their results, i.e., we re-nondimensionalized their spectra results in order to maintain consistency between spectra and structure function (we chose this estimate as it does not rely on the C_k value, which can be contaminated by the low Reynolds number of the $Re_\lambda \approx 600$ case, see discussion in Sect. 4.3).

3.2 Meyers and Meneveau (2008)

To help with data interpretation, we use the model three-dimensional spectrum proposed by Meyers and Meneveau (2008). The model updates previous theoretical models based on the inertial and dissipation decay rates by incorporating the bottleneck and intermittency effects as observed in DNS, laboratory and atmospheric data. The three dimensional spectrum $E(\kappa)$ is defined as the contribution to the turbulent kinetic energy from all wavenumbers with absolute value κ , and the proposed model corresponds to:

$$E(\kappa) = C_k \varepsilon^{2/3} \kappa^{-5/3} (\kappa L)^{-\beta} f_L(\kappa L) f_\eta(\kappa \eta), \quad (6)$$

$$f_L(\kappa L) = \left\{ \frac{\kappa L}{[(\kappa L)^p + \alpha_5]^{1/p}} \right\}^{5/3 + \beta + 2}, \quad (7)$$

$$f_\eta(\kappa \eta) = \exp(-\alpha_1 \kappa \eta) \left[1 + \frac{\alpha_2 (\kappa \eta / \alpha_4)^{\alpha_3}}{1 + (\kappa \eta / \alpha_4)^{\alpha_3}} \right], \quad (8)$$

in which C_k is the Kolmogorov constant, ε is the turbulence kinetic energy dissipation rate, L is the integral length scale, β is the intermittency correction for the inertial-range slope, $\eta = (\nu^3/\varepsilon)^{1/4}$ is the Kolmogorov (dissipation) length scale, in which ν is the kinematic viscosity, and f_L and f_η are non-dimensional functions representing the integral and dissipation scales, respectively. The main contributions from this approach compared to other spectrum models (such as Pope (2000)'s) are the parameterization of the intermittency and bottleneck effects, the later being the spectral bump at the transition between the inertial and dissipation scales (modeled by the term multiplying the exponential function in Eq. 8).

In addition to the flow scales and parameters, the values of α_1 – α_5 need to be determined in order to close the model. For a given Reynolds number, five flow constraints are used to obtain these constants, namely the total energy, entropy and palinstropy from their corresponding integrals of the energy spectrum ($E(\kappa)$, $\kappa^2 E(\kappa)$ and $\kappa^4 E(\kappa)$, respectively), combined with the constraint for the magnitude and location of the intermittency corrected dissipation peak (equations 6–8 and 11 of the original study). From the field data we extract the Reynolds number, dissipation rate, and the derivative skewness S_3 (needed for the palinstropy constraint, see Meyers and Meneveau (2008) for details). The values of $p = 1.5$, $\beta = \mu/9$ ($\mu = 0.25$ is the standard empirical value of intermittency exponent) were selected as in Meyers and Meneveau (2008). The value of the Kolmogorov constant $C_k = 2.3$ was used as in the modeling of atmospheric data from Tsuji (2004) by Meyers and Meneveau (2008). Table 2 provides the model parameters for the present data in addition to the results of the field data provided by Tsuji (2004) (discussed in Sect. 4.3), obtained using the GNU Octave software (Eaton et al. 2020).

Note that from this model, the behavior in the inertial range deviates from Kolmogorov's law, especially if the Reynolds number is very large (so that κL is large in the inertial range). However, if the spectrum is normalized according to Kolmogorov's law, it will require a different constant, i.e., $E(\kappa) = C'_k \varepsilon^{2/3} \kappa^{-5/3}$. Here, $C'_k = C_k (\kappa_{\text{IR}} L)^{-\beta} f_\eta(\kappa_{\text{IR}} \eta)$ and κ_{IR} is a wavenumber representative of the inertial range (Meyers and Meneveau 2008). Therefore, the value of $C_k = 2.3$ should not be used directly in Kolmogorov's law.

From Meyers and Meneveau (2008)'s model, the following relations are used to obtain the one-dimensional energy spectra (the contribution of the streamwise wavenumber k_1 to each corresponding variance) and second- and third-order structure functions for each velocity component (Pope 2000):

Table 2 Parameters of the Meyers and Meneveau (2008)’s model estimated for the present data and for the data from Tsuji (2004). As in Meyers and Meneveau (2008), the values of $C_k = 2.3$, $p = 1.5$, $\beta = \mu/9$ and $\mu = 0.25$ were used, in addition to the measured value of S_3 for the present data (italic), and calculated from $S_3 = C_3 Re_\lambda^{9\mu/16}$ for $C_3 = -0.146$ (upper bound, corresponding to the S_3 measured in this study) and -0.218 (lower bound, corresponding to the value used by Meyers and Meneveau (2008) for Tsuji (2004)’s data). Mean velocity \bar{u}_1 in [m s⁻¹] and mean dissipation rate ε in [m² s⁻³]

	present	Tsuji (2004)				
\bar{u}_1	2.21	2.82	5.16	5.67	7.66	
ε	0.00488	0.0106	0.0840	0.0598	0.0760	
Re_λ	1550	5940	12240	15630	21180	
Upper bound						
S_3	<i>-0.41</i>	-0.50	-0.55	-0.57	-0.59	
α_1	6.64352	5.42477	4.96725	4.83118	4.67283	
α_2	9.57462	4.14483	3.11842	2.87126	2.61096	
α_3	1.53194	1.73657	1.89901	1.96447	2.05451	
α_4	0.31066	0.17458	0.14447	0.13712	0.12945	
α_5	5.73480	5.80286	5.82066	5.82470	5.82867	
Lower bound						
S_3	-0.61	-0.74	-0.82	-0.85	-0.88	
α_1	4.46575	4.00902	3.79519	3.72710	3.64518	
α_2	1.74661	1.44918	1.32980	1.29424	1.25301	
α_3	6.43234	10.55001	15.49512	18.24595	23.17269	
α_4	0.12115	0.12863	0.13551	0.13835	0.14227	
α_5	5.57008	5.76794	5.80600	5.81379	5.82113	

$$E_{11}(k_1) = \int_{k_1}^\infty \frac{E(\kappa)}{\kappa} \left(1 - \frac{k_1^2}{\kappa^2}\right) d\kappa, \tag{9}$$

$$E_{22}(k_1) = E_{33}(k_1) = \frac{1}{2} \left(E_{11}(k_1) - k_1 \frac{dE_{11}(k_1)}{dk_1} \right), \tag{10}$$

$$D_{\gamma\gamma}(r_1) = 2 \int_0^\infty E_{\gamma\gamma}(k_1) [1 - \cos(k_1 r_1)] dk_1, \quad \gamma = 1, 2 \text{ or } 3, \tag{11}$$

$$D_{111}(r_1) = -\frac{4}{5} \varepsilon r_1 + 6v \frac{dD_{11}(r_1)}{dr_1}, \tag{12}$$

$$D_{122}(r_1) = D_{133}(r_1) = \frac{1}{6} \left(r_1 \frac{dD_{111}(r_1)}{dr_1} + D_{111}(r_1) \right), \tag{13}$$

in which r_1 is the separation distance in the longitudinal direction. The structure functions are defined as:

$$D_{\gamma\gamma} = \overline{[u_\gamma(x_1 + r_1) - u_\gamma(x_1)]^2}, \tag{14}$$

$$D_{\gamma\omega\omega} = \overline{[u_\gamma(x_1 + r_1) - u_\gamma(x_1)][u_\omega(x_1 + r_1) - u_\omega(x_1)]^2}. \tag{15}$$

Note that Eqs. (9), (10) and (13) are only valid for locally homogeneous and isotropic flows, whereas Eq. (12), from the Kármán-Howarth equation, requires the additional constraint of stationarity (Hill 1997). Therefore the model predictions presented here are only meaningful within the scales for which local isotropy is a reasonable assumption. All hot-film results presented next are accompanied by model predictions to facilitate the discussion.

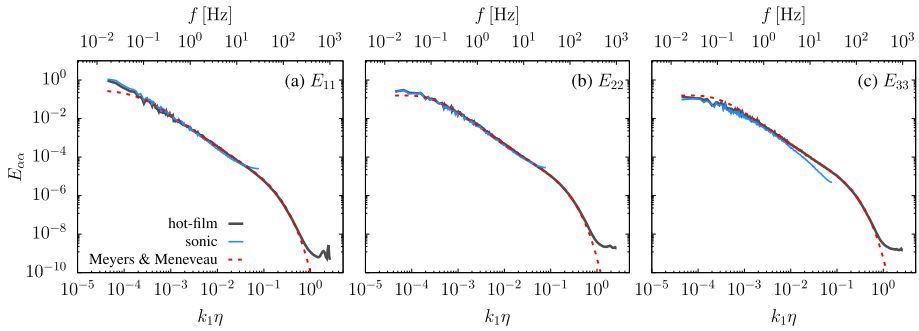


Fig. 5 One-dimensional spectra for the (a) streamwise, (b) spanwise and (c) vertical velocities as a function of the streamwise nondimensional wavenumber and frequency. Spectra were smoothed using bin averages in log scale, and Taylor’s frozen turbulence hypothesis was used. Hot-film (grey) and sonic (blue) anemometers data, in addition to Meyers and Meneveau (2008)’s model (dashed red lines)

4 Results

The one-dimensional spectra in the streamwise direction for each velocity component are presented in Fig. 5. As done in previous *in situ* calibration studies (Kit et al. 2010; Singha and Sadr 2013), visual inspection of the spectra combined with the time series of Fig. 4 indicates a successful calibration. A quantitative error estimation is provided in the Appendix, showing that, although the sonic data is not an ideal “ground truth” velocity in this case due to the sensors’ misalignment, the errors are in the range of previous *in situ* calibration studies. Here, a more detailed comparison of the small scales is provided, including compensated spectra and structure functions and isotropy ratios, presented in log-linear graphics (as opposed to log-log graphics typically used in the literature) in order to emphasize similarities and discrepancies. Note that the range of the spectra used for calibration of the hot-film data ($f \leq 0.05$ Hz) is barely included in the data analysis presented hereafter (see Fig. 5), because the size of the subblocks (2 min) limits estimates of such low frequencies (see Appendix for further discussion).

4.1 Spectra

Figure 6 compares dissipation spectra between hot-film and Meyers and Meneveau (2008)’s model for each velocity component. Since they were independently derived, the similar behavior between model and observations serve as another indication of the successful data calibration. It also shows that the model captures fairly well the position and shape of the peaks in dissipation, which are associated with the spectral bump at $k_1\eta \approx 0.1$. By construction, the model and data should have the same total rate of dissipation (as this is one of the input parameters used in the model). Because the model assumes isotropy, the overprediction in the streamwise component (mostly compensated by under prediction in the spanwise component, Fig. 6(a,b)) signals deviations from isotropy at the dissipation scales in the hot-film data. This is in part associated with properties of the spectral bump as discussed further below.

When the energy spectra are compensated using Kolmogorov’s scaling (i.e., premultiplied by $k_1^{5/3}$), we can identify roughly one decade of inertial range behavior in the streamwise component (Fig. 7a), which does not seem to display a spectral bump. In the other two

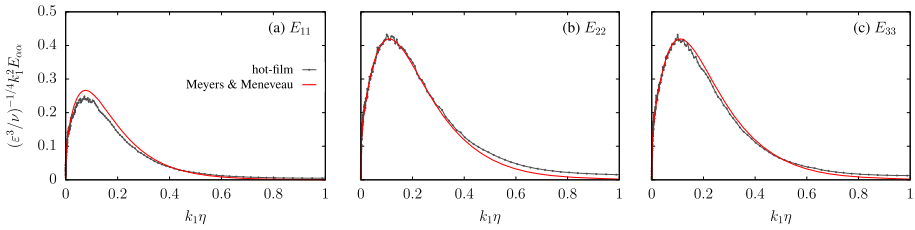


Fig. 6 Dissipation spectra for the (a) streamwise, (b) spanwise and (c) vertical velocities as a function of the nondimensional wavenumber. Hot-film data in grey and Meyers and Meneveau (2008)’s model in red. The mean dissipation rate was estimated as the average of the integrals of these three data curves (Eq. 5)

components (Fig. 7b, c), the presence of spectral bumps prevent the formation of a clear inertial range at this fairly low Reynolds number. When comparing spectra from the sonic with those from hot-film, the sonic path-averaging and aliasing effects become quite clear, the former being most significant in the vertical component (which has the larger path length). It is important to emphasize that the errors associated with sonic anemometer, including path averaging (Horst and Oncley 2006) and flow distortion by transducer shadowing (Horst et al. 2015), are influenced by the incident wind angle, and the $\sim 90^\circ$ angle used in this study enhances the degradation of the sonic data (these errors tend to be substantially smaller for angles within $\pm 45^\circ$). For that reason, we avoid placing too much emphasis on the limitations of the sonic anemometer as a more meaningful comparison would require both sensors to be pointing in the same direction (so that the incidence angle is the same).

The best comparison between data and model is also given by the compensated spectra (premultiplied $\kappa_1^{5/3+\beta}$ in Fig. 7d–f). Note that here we use the intermittency correction in the compensated spectra to properly identify the existence of the inertial range in the model. While the model predicts a bump in all three velocity components (less pronounced in E_{11}), the data follows the model closely in the large wavenumbers only in the spanwise and vertical directions, for which a clear spectral bump is present. The lack of a bump in E_{11} obtained from the hot-film, whose cause cannot be inferred from this dataset, is likely influencing the observed dissipation spectra anisotropy and the 2.2 value obtained for the isotropy ratios of the velocity derivative variance (Fig. 2), since the peak in the dissipation spectra approximately coincides with the end of the peak in the bump. Except for the lack of a spectral bump in E_{11} , the only other clear difference between the data and the model is in the energy-containing range ($k_1\eta \lesssim 10^{-3}$) for E_{33} , where the hot-film closely follows the sonic. This reduction in the energy-containing scales of E_{33} is expected as the vertical velocity is significantly impacted by the blocking of the flow by the ground, making the integral scales quite anisotropic and violating the model assumptions in this range of scales. Figure 7 also includes an empirical fit to the wind-tunnel data (ninth-order, least-square, log-log polynomial fits) as presented by Saddoughi and Veeravalli (1994). Compared to the atmospheric data with similar Re_λ evaluated here, the Saddoughi and Veeravalli (1994) data presents a more pronounced bump in both streamwise and vertical components and some differences in the production range, but the overall agreement with the model is quite good.

The ratios between components of the one-dimensional spectra are usually employed to assess the validity of local isotropy and are presented in Fig. 8, which further characterizes the inertial range behavior and the similarity between hot-film data and Meyers and Meneveau (2008)’s model. The local isotropy predictions for the inertial range ($E_{22}/E_{11} = E_{33}/E_{11} = 4/3$ and $E_{33}/E_{22} = 1$) are also indicated. Note that the isotropic model predicts the ratios

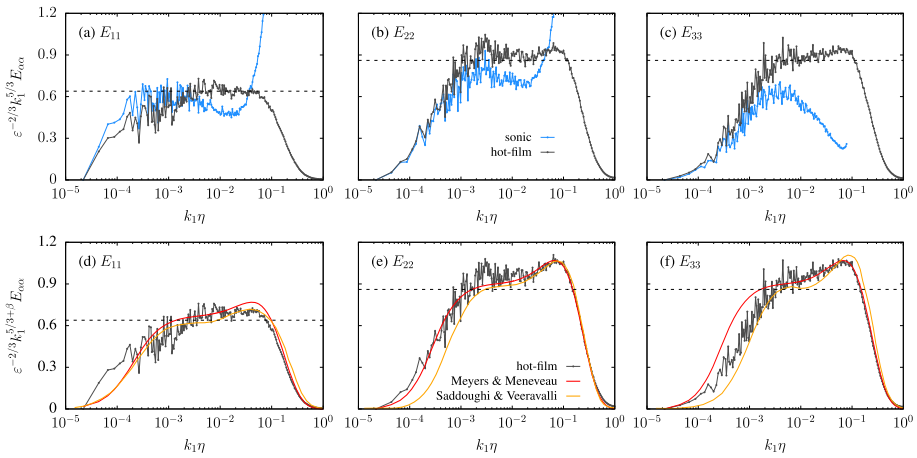


Fig. 7 Compensated one-dimensional spectra of (a, d) streamwise, (b, e) spanwise, (c, f) vertical velocities as a function of the nondimensional wavenumber. Hot-film/sonic data in grey/blue lines, Meyers and Meneveau (2008)’s model and Saddoughi and Veeravalli (1994)’s data in red/yellow lines. The dashed black horizontal lines correspond to the theoretically predicted values for the inertial range

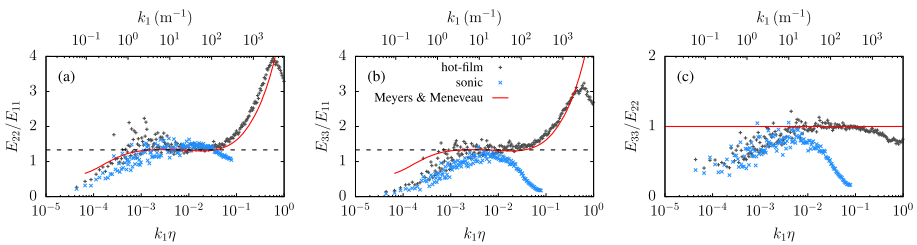


Fig. 8 Ratios of the one-dimensional spectra. Hot-film/sonic anemometers data in grey/blue crosses, in addition to Meyers and Meneveau (2008)’s model (red lines). The dashed black horizontal lines correspond to the theoretically predicted 4/3 value for the inertial range

between transverse components to the streamwise component to be larger than 4/3 in the dissipation range. In general, the agreement between data and model in the inertial range and in the dissipation range confirm that the local isotropy assumption is reasonably justified. The sonic anemometer seems to have limitations that prevent an adequate assessment of local isotropy, especially when the vertical component is included. This conclusion was also obtained by Peña et al. (2019), in particular for the Campbell CSAT3 anemometer, whose ratio E_{33}/E_{11} was at most 1.2 even after accounting for flow-distortion effects. Therefore, if this type of behavior for sonic data is confirmed at larger Reynolds numbers and different angles of incidence, then caution should be taken when using CSAT3 in the assessment of local isotropy in the inertial range.

4.2 Structure Functions

Evaluation of the second-order structure function is more sensitive to small differences between sonic, hot-film, and model results, given that it corresponds to an integral of the spectrum (Eq. 11). Figure 9 (upper panels) reinforces the similarity between hot-film, model

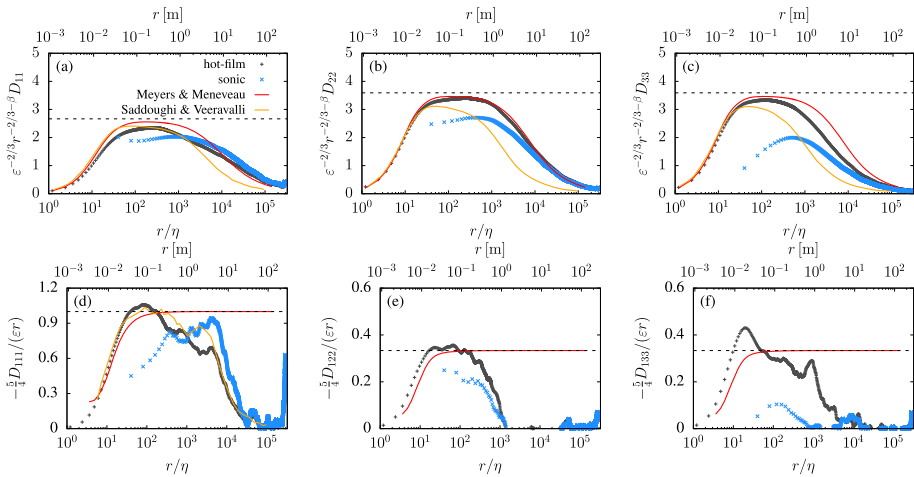


Fig. 9 Nondimensionalized second- (upper panels) and third- (lower panels) order structure functions ((a, d) streamwise, (b, e) spanwise, (c, f) vertical). Hot-film/sonic anemometers data as grey/blue crosses, in addition to Meyers and Meneveau (2008)’s model and Saddoughi and Veeravalli (1994)’s data in red/yellow lines. The dashed black horizontal lines correspond to the theoretically predicted values for inertial range

and wind-tunnel data in the dissipation range, in addition to the similarity between hot-film and model across all scales in the spanwise component D_{22} . The discrepancies discussed in the context of the spectra are amplified here. The absence of a spectral bump in E_{11} for the hotfilm data manifests in lower values of observed values of D_{11} when compared to the model. Second-order structure functions exacerbate the sonic anemometer’s poor performance, because the sonic cannot sample the smallest scales in the flow and the structure function represents energy accumulated from the smallest scales up to r . Note that it takes between one and two decades of r/η for the structure functions obtained from the sonic to converge to the hot-film values. Another noteworthy aspect of the structure functions for the present value of Re_λ is that both data (our hot-film data as well as those from Saddoughi and Veeravalli (1994)) and model differ from the prediction for the inertial range (dashed lines) obtained from the integral of the spectra assuming an infinitely long Kolmogorov inertial range. The similarity between the model and wind tunnel data indicates that this issue is not related to canopy or stratification effects, rather this issue is most likely another effect of the spectral bump in these measurements with limited Reynolds number. Section 4.3 investigates this issue in more details.

The third-order structure function (Fig. 9 lower panels) is more difficult to accurately calculate, as it requires longer time averaging to converge compared to the second-order counterpart (Kaimal and Finnigan 1994; Podesta et al. 2009). Note that model estimates for all three third-order structure functions are based on D_{11} only (in Eq. 12, D_{22} and D_{33} are never used), and the overprediction of the growth of D_{11} with r in the dissipation range (see Fig. 9a) compromises the agreement between model and data for the third order structure functions. It is difficult to determine whether hot-film data is impacted by the small sample size for $(r/\eta) > 10^2$. Clearly the sonic data is not able to provide reliable values of the third-order structure function for this dataset, probably due to the sensor’s path-averaging and flow distortion errors. Note that the second-order structure function from the sonic starts deviating from the hot-film around $r/\eta \sim 10^{-4}$, and that the third order structure function is likely much more sensitive to small flow distortions than the second-order counterparts.

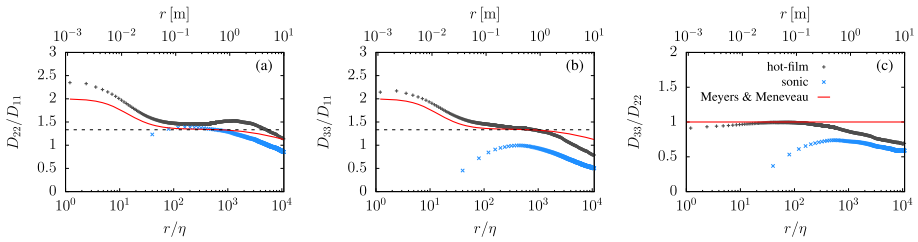


Fig. 10 Ratios of the second-order structure functions. Hot-film (grey) and sonic (blue) anemometers data, in addition to Meyers and Meneveau (2008)’s model (red lines). The dashed black horizontal lines correspond to the theoretically predicted values for the inertial range

The isotropy ratios of the second-order structure functions (Fig. 10) are also impacted by the anisotropy in the spectral bump. The only ratio that is not impacted much is D_{33}/D_{22} , which is in agreement with predictions from local isotropy for more than half a decade of scales. It is very interesting that the sonic data conforms reasonably well to the isotropy ratio of D_{22}/D_{11} , despite producing values of the second-order structure functions much lower than those from the hot-film.

4.3 Reynolds Number Dependence of the Inertial Range

The theoretical behavior of the inertial range when $Re_\lambda \rightarrow \infty$, as defined by Kolmogorov’s law, is commonly used as an indirect estimate of the dissipation rate when only sonic data are available. Because results from the present analyses raise concerns regarding the length and magnitude of the inertial range, in particular of the structure function, it is important to investigate the impact of the finite Re_λ on the inertial range for realistic atmospheric turbulence conditions.

For large enough Re_λ , the behavior of the energy spectrum in the inertial range should follow $C_k L^{-\beta} \varepsilon^{2/3} \kappa^{-p}$, $p = 5/3 + \beta$ (from Eq. 6), as the functions f_L and f_η should be approximately one. For the one-dimensional spectra $E_{\alpha\alpha}$, this will correspond to a similar behavior $C_\alpha L^{-\beta} \varepsilon^{2/3} \kappa^{-p}$, in which $C_1 = C_k / (0.5p(2 + p))$ and $C_2 = 0.5(1 + p)C_1$ (Pope 2000, p. 228). Without intermittency, $\beta = 0$, $p = -5/3$ and the usual $C_1 = 18C_k/55$ and $C_2 = 4C_1/3$ are obtained. If intermittency is considered, the value of $p = -5/3 - \beta$ should be taken into account, which corresponds to $C_1 = 2592C_k/8113$ and $C_2 = 97C_1/72$. Although these intermittency corrections are small (since $\beta = 1/36$), they are not negligible, as it will be shown next.

For the second-order structure functions, the inertial range behavior corresponds to $D_{\gamma\gamma} = C_\gamma^* L^{-\beta} \varepsilon^{2/3} r^q$ (from Eq. 11), with $q = p - 1$ and $C_1/C_1^* = \Gamma(1 + q) \sin(\pi q/2)/\pi$ (Pope 2000, p. 701). Without intermittency, $\beta = 0$, $q = 2/3$, $C_1^* \approx 4C_1$ and $C_2^* = 4C_1^*/3$. With intermittency, $q = 2/3 + \beta$, $C_1^* \approx 3.9C_1$ and $C_2^* = 97C_1^*/72$, a less negligible correction since q is closer to β compared to p .

In order to investigate the effect of Re_λ on the inertial range behavior, we use the Meyers and Meneveau (2008)’s model combined with the atmospheric data from Tsuji (2004). The field data and corresponding model’s parameters are provided in Table 2. Because the value of S_3 was not provided with the published data, and since there is no clear consensus regarding the behavior of $S_3(Re_\lambda)$ (Sreenivasan and Antonia 1997) especially for atmospheric data (Djenidi et al. 2017), we chose to adjust the model used by Meyers and Meneveau (2008), namely $S_3 = C_3 Re_\lambda^{9\mu/16}$ to the value $S_3(Re_\lambda = 1550) = -0.41$ obtained here as an upper

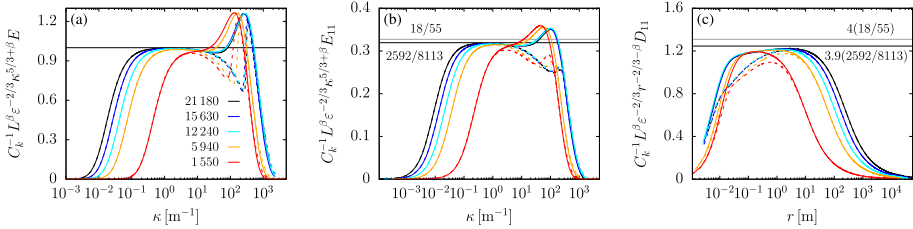


Fig. 11 Meyers and Meneveau (2008)’s model results for the atmospheric data including Tsuji’s (2004) data. (a) Three-dimensional spectrum, (b) streamwise 1D spectrum and (c) longitudinal second-order structure function, for $Re_\lambda = 21\,180$ (black), $15\,630$ (blue), $12\,240$ (cyan), $5\,940$ (orange) and $1\,550$ (present data, red), using $S_3 = C_3 Re_\lambda^{9\mu/16}$ and $C_3 = -0.146$ (upper bound, solid) and -0.128 (lower bound, dashed). Horizontal lines correspond to the theoretically predicted values for the inertial range without (grey) and with (black) intermittency

bound, and $S_3(Re_\lambda = 17060) = -0.86$ obtained by Meyers and Meneveau (2008) for Tsuji (2004) data as a lower bound, as described in Table 2. These two curves approximately form an envelope around the $S_3(Re_\lambda)$ data presented by Sreenivasan and Antonia (1997) (Fig. 5) for $Re_\lambda \gtrsim 500$.

Figure 11 shows the model predictions, assuming a 2 h time series with 2 kHz measurement frequency (to improve conversion of both large and small scales). For 3D spectra, it is possible to observe the extent of the impact of the value of S_3 , which starts at $\kappa \approx 20\text{ m}^{-1}$. According to this model, the inertial range extends at most one decade for the highest Re_λ evaluated here, regardless of the value of S_3 used. In the upper limit of S_3 , the deviation in the inertial range caused by the bump is less pronounced (and possibly masked in log-log plots), but still present. For $Re_\lambda = 5\,940$ the inertial range plateau is already impacted by the production/dissipation ranges of the spectrum, not reaching the C_k value imposed. For the present data ($Re_\lambda = 1\,550$) Meyers and Meneveau’s (2008) model suggests that the inertial range is most likely absent, as discussed previously.

A similar inertial region exists for the one-dimensional spectrum (Fig. 11b), and the impact of the intermittency correction on the constant can be seen as small but non-negligible. Finally, the second-order structure function (Fig. 11c) does not reach the theoretically predicted values for the inertial range even for $Re_\lambda = 21\,180$ (despite the constant being significantly reduced by the intermittency correction). Although the limitation is caused by the length of the inertial range, it is possible to see that it is particularly penalized by the large-scale range (since the small scales are very similar for the largest three Re_λ cases). The difference to the structure function prediction can be considered small for high-Reynolds number flows, but the lack of a clear inertial range in the structure function is remarkable. Furthermore, for Re_λ smaller than ~ 5000 , as in the present data, this difference can be significant and it needs to be taken into account. Overall, this analysis indicates that finite Reynolds number effects on spectra and structure functions could be more ubiquitous in atmospheric flows than commonly assumed.

5 Conclusions

In this study we test an *in situ* calibration of hot-film data measured above a walnut orchard, using simultaneous sonic anemometer data. The method was developed based on the idea that the sonic data can be used as a replacement for the known velocity typically used in the calibration process. The method overcomes the need of constant recalibration of the sen-

sor during the field experiment, relying only on properties of the sensors (yaw and pitch parameters, geometry and relative position) and a physics-based relationship (namely King's law, as opposed to a numerical transfer function provided by a neural network method). As a downside, we note that the present method is very sensitive to small errors, as indicated by the effect of angle error on isotropy ratios (Fig. 2), which would likely be automatically corrected by the numerical transfer function in the neural network method. Because hot-film anemometers require a consistent flow direction, which is particularly difficult to achieve above a canopy due to strong turbulence intensities, it was not possible to obtain long consecutive periods of data satisfying the quality-control criteria. Nevertheless, it was possible to calibrate the hot-film using one long 3-hour period and to produce 33 2-min subblocks of hot-film data not contaminated by data with higher wind direction angles, and yielding reasonably converged statistics. The subblocks of data without error gaps provided by this traditional calibration method is an upside compared to the neural network method, whose effect of high turbulence intensity on small-scale statistics still needs investigation.

To evaluate the quality of those statistics and validate the calibration method, we compared the results with wind-tunnel data of Saddoughi and Veeravalli (1994) (of similar Re_λ), and with the model spectra of Meyers and Meneveau (2008). The generally similar spectrum and structure function results provide some confidence on the calibration technique, as most of the discrepancies can be attributed to flow condition differences and on having assumed isotropy.

Our dataset suggests that the spectral bump in the energy spectrum is anisotropic, with the streamwise component having less energy than the other two components. It is entirely possible that this difference arises due to distortions caused by the use of Taylor's hypothesis, the presence of the canopy or the stable stratification, something that cannot be investigated with the present data. The presence of the spectral bump and, in particular, its anisotropy, have many consequences for isotropy in the inertial range, especially at low Re_λ investigated here. Only a limited region that can be identified as the inertial range exists in the streamwise spectrum (in which the bump is very small or non-existent), while no clear inertial range exists for the other two velocity components. The scales that conform more closely to inertial range scaling are impacted by the bump and its anisotropy (this impacts both scalings and isotropy ratios). The effect of the bump is amplified in the second-order structure function, and its anisotropy produces much larger deviations than it is the case in the spectra.

The comparison with the model spectra provides an important additional insight: the structure function, by definition, cannot reach the prediction of infinitely large inertial range unless the Re_λ is sufficiently high. This remark, already discussed by Sreenivasan and Dhruva (1998) for atmospheric flow and recently by Antonia et al. (2019) for different types of flows, should be taken into account when using the inertial range of the structure function for flow predictions, such as the indirect estimation of the dissipation rate. Hot-film anemometry data can provide a useful alternative in this regard.

Finally, one of the original goals of this study was to investigate the quality of the sonic anemometer data in the inertial range, especially as sonic data is often used for indirect estimation of the dissipation rate. However, due to the experimental setup with an 85° angle between the two sensors, the sonic anemometer measurements are outside the ideal range for the sensor and likely include more errors than for smaller angles. If the data presented here provides any indication of the performance of sonic anemometers in the inertial range, the results are quite discouraging, in particular for canopy flows. If the hot-film data are to be trusted, then the dissipation estimated from the streamwise spectrum by the sonic anemometer would be slightly lower than the true value. All other estimates would be far off. In particular, the second-order structure functions would produce a very large underestimation

of the dissipation rate despite showing proper inertial range scaling. Furthermore, when close enough to the ground, the CSAT3 data has a damped inertial range in all second-order structure functions (D_{11} , D_{22} and D_{33}), which is more pronounced in D_{33} leading to wrong isotropy ratios. This is a cause for concern, since scaling and isotropy are frequently used as measure of the reliability of the data. A more carefully designed field experiment is needed to address some of these questions, ideally including a pre-calibration of the hot-film probe to check all calibration parameters, and a method for reorientation of the sensors in the field (as already present in the combo probe by Goldshmid et al. (2022), for example).

Acknowledgements The authors thank Steve Oncley and Gary Granger of NCAR's Earth Observing Laboratory for fruitful discussions and their assistance in accessing the CHATS hot-film anemometry data, and the Cilker family for allowing the CHATS experiment to take place in their orchard. We thank the anonymous reviewers for important observations and suggestions.

Author Contributions E.G.P. participated in the data collection and preparation. L.S.F. and M.C. performed the data analysis and wrote the first draft of the manuscript. All authors provided critical feedback and helped shape the research, analysis and manuscript.

Funding L.S.F. was funded by the São Paulo Research Foundation (FAPESP, Brazil), Grants No. 2018/24284-1 and 2019/14371-7. This material is based upon work supported by the National Center for Atmospheric Research, which is a major facility sponsored by the National Science Foundation under Cooperative Agreement No. 1852977. E.G.P. acknowledges supplemental support from NCAR's Geophysical Turbulence Program.

Availability of data and materials The datasets generated during and/or analysed during the current study are available from the corresponding author on reasonable request.

Declarations

Ethical Approval Not applicable.

Competing interests The authors have no conflict of interest, financial or otherwise.

Appendix: Illustration of the Calibration Procedure and Additional Statistics

The data processing required two steps, an initial data selection and a final data selection. The initial data selection consisted of going through all available data, and selecting the 30-min blocks that passed two quality criteria: mean wind direction relative to the hot-film's orientation smaller than 10° and a final number of 30-sec subblocks of at least 25. This stage was repeated correcting for angles $80^\circ \leq \theta_z \leq 90^\circ$, when the value of $\theta_z = 85^\circ$ was selected.

The final data selection consisted of a single 3-hour block, from which 33 subblocks of 2-min data without gaps were identified. These data were selected in order to increase the subblock length and the statistical convergence in the average between subblocks. It was also the only long period of several consecutive blocks that passed the initial data screening. See a summary in Fig. 12.

Figure 12 also illustrates the concept of blocks and subblocks. While the original data (hot-film voltage and sonic velocity) was separated in blocks (30-min and 3 hours long for the initial and final data selection, respectively), the final hot-film velocity presented gaps in the time series. Consecutive periods of data without gaps (30-sec and 2-min long for the

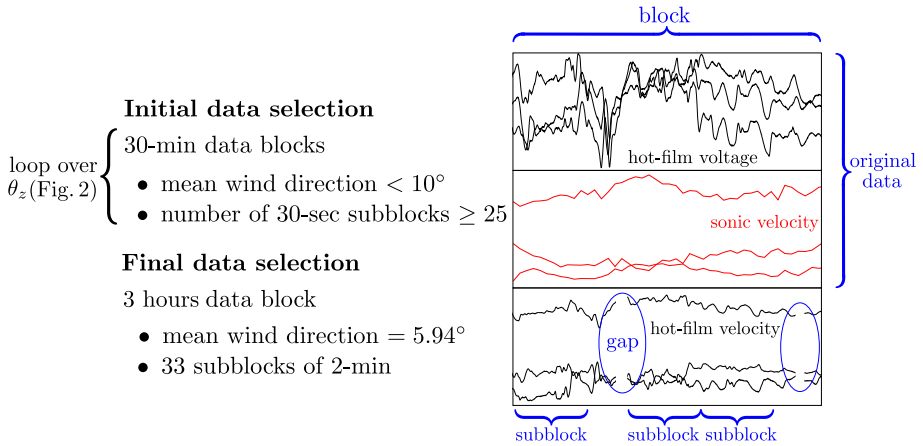


Fig. 12 Summary of data selection and illustration of the blocks and subblocks used in this study. While the block consisted of a fixed period in the original data (hotfilm voltage and sonic velocity, 30-min and 3-hours long), the subblocks were formed in the final hot-film velocity series by selecting consecutive periods without gaps

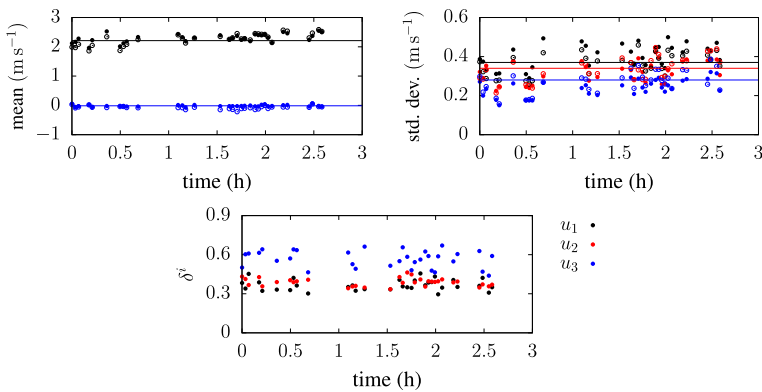


Fig. 13 Block average (3 hours, solid lines) versus subblocks statistics (2-min, circles). Filled (open) circles are sonic (hot-film) data. Mean (top left), standard deviation (top right) and delta parameter (bottom) of the streamwise (black), spanwise (red) and vertical (blue) velocities

initial and final data selection, respectively) were then selected as subblocks, which can start at the beginning of a block, immediately after a gap or after another subblock.

Figure 13 shows the mean and standard deviation of the three velocity components for each subblock, compared to the 3-hour value and comparing between sonic and hot-film values. Results show that the flow presented a slight increase in mean velocity and standard deviation over time, but it can be considered approximately steady-state, justifying the average over subblocks of all statistics presented in this study.

In order to compare sonic and velocity data directly, it is important to filter both data at the frequencies in which they are comparable. As discussed in Sec. 2.5, ideally, at most a 0.3 Hz cut-off frequency should be used (see Fig. 3). However, a 2-min time series at 0.3 Hz of frequency has only 36 data points, which are not statistically meaningful. Instead, we filtered the two datasets at 2 Hz, see Fig. 14. Notice that, at this frequency, the sonic data already

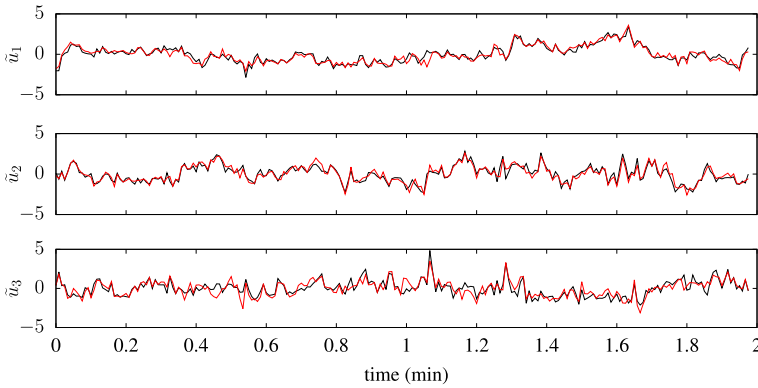


Fig. 14 Time series of the filtered and rescaled velocity vector (filtered at the 2 Hz frequency, rescaled by their mean and standard deviation of the subblock) of the hot-film (black) and sonic (red) data, for the last 2 min block

diverges from the hot-film data, which can be seen in Fig. 14. Furthermore, we estimated the delta parameter as a quantitative measurement of the difference between the two time series (Kit and Liberzon 2016; Goldshmid et al. 2022). The delta parameter is defined as:

$$\delta^i = \left\{ \frac{1}{N} \sum_{j=1}^N (\tilde{u}_{h,i}^{(j)} - \tilde{u}_{s,i}^{(j)})^2 \right\}^{1/2}, \tag{16}$$

where $\tilde{u}_i^{(j)}$ is the j^{th} value of the velocity component i filtered at 2 Hz and rescaled by their mean and standard deviation values of the subblock (subscripts s and h are for sonic and hot-film, respectively). The values of δ^i are presented in Fig. 13, varying from 0.3 to 0.7. These values are relatively high but of the same order of magnitude of the values obtained by Kit and Liberzon (2016) and Goldshmid et al. (2022) using both traditional and neural network calibration. We expect that in a more favorable setup, such as sonic pointing to the streamwise direction, the sonic velocity would correspond to a better “ground truth” for the velocity fluctuation and the δ^i values would be lower.

References

Amiro BD (1990) Drag coefficients and turbulence spectra within three boreal forest canopies. *Boundary-Layer Meteorol* 52(3):227–246

Antonia RA, Tang SL, Djenidi L, Zhou Y (2019) Finite Reynolds number effect and the 4/5 law. *Phys Rev Fluids* 4(084):602. <https://doi.org/10.1103/PhysRevFluids.4.084602>

Baldocchi DD, Meyers TP (1988) A spectral and lag-correlation analysis of turbulence in a deciduous forest canopy. *Boundary-Layer Meteorol* 45(1):31–58

Cava D, Katul GG (2008) Spectral short-circuiting and wake production within the canopy trunk space of an alpine hardwood forest. *Boundary-Layer Meteorol* 126(3):415–431

Djenidi L, Antonia RA, Talluru MK, Abe H (2017) Skewness and flatness factors of the longitudinal velocity derivative in wall-bounded flows. *Phys Rev Fluids* 2(064):608. <https://doi.org/10.1103/PhysRevFluids.2.064608>

Dupont S, Patton EG (2012) Influence of stability and seasonal canopy changes on micrometeorology within and above an orchard canopy: the CHATS experiment. *Agric Forest Meteorol* 157:11–29. <https://doi.org/10.1016/j.agrformet.2012.01.011>

- Dupont S, Patton EG (2022) On the influence of large-scale atmospheric motions on near-surface turbulence: comparison between flows over low-roughness and tall vegetation canopies. *Boundary-Layer Meteorol* 184(2):195–230. <https://doi.org/10.1007/s10546-022-00710-z>
- Eaton JW, Bateman D, Hauberg S, Wehbring R (2020) GNU Octave version 5.2.0 manual: a high-level interactive language for numerical computations
- Finnigan J (2000) Turbulence in plant canopies. *Ann Rev Fluid Mech* 32(1):519–571. <https://doi.org/10.1146/annurev.fluid.32.1.519>
- Frehlich R, Meillier Y, Jensen ML, Balsley B (2003) Turbulence measurements with the cires tethered lifting system during cases-99: calibration and spectral analysis of temperature and velocity. *J Atmosph Sci* 60(20):2487–2495. [https://doi.org/10.1175/1520-0469\(2003\)060<2487:TMWTCT>2.0.CO;2](https://doi.org/10.1175/1520-0469(2003)060<2487:TMWTCT>2.0.CO;2)
- Goldshmid RH, Winiarska E, Liberzon D (2022) Next generation combined sonic-hotfilm anemometer: wind alignment and automated calibration procedure using deep learning. *Exp Fluids* 63(1):30
- Gulitski G, Kholmyansky M, Kinzelbach W, Lüthi B, Tsinober A, Yorish S (2007) Velocity and temperature derivatives in high-reynolds-number turbulent flows in the atmospheric surface layer. Part 1. Facilities, methods and some general results. *J Fluid Mech* 589:57–81. <https://doi.org/10.1017/S0022112007007495>
- Hasse L, Dunckel M (1980) Hot wire and hot film anemometers. Springer: US, Boston, MA, pp 47–63. https://doi.org/10.1007/978-1-4615-9182-5_3
- Hill RJ (1997) Applicability of Kolmogorov's and Monin's equations of turbulence. *J Fluid Mech* 353:67–81. <https://doi.org/10.1017/S0022112097007362>
- Horst TW, Oncley SP (2006) Corrections to inertial-range power spectra measured by Csat3 and solent sonic anemometers. I. Path-averaging errors. *Boundary-Layer Meteorol* 119(2):375–395. <https://doi.org/10.1007/s10546-005-9015-7>
- Horst TW, Semmer SR, Maclean G (2015) Correction of a non-orthogonal, three-component sonic anemometer for flow distortion by transducer shadowing. *Boundary-Layer Meteorol* 155(3):371–395. <https://doi.org/10.1007/s10546-015-0010-3>
- Jørgensen FE (2005) How to measure turbulence with hot-wire anemometers—a practical guide. Dantec Dynamics, Tonsbakken
- Kaimal JC, Finnigan JJ (1994) Atmospheric boundary layer flows: their structure and measurement. Oxford University Press, Oxford
- Kelly M, Wyngaard JC (2006) Two-dimensional spectra in the atmospheric boundary layer. *J Atmosph Sci* 63(11):3066–3070. <https://doi.org/10.1175/JAS3769.1>
- Kit E, Liberzon D (2016) 3d-calibration of three- and four-sensor hot-film probes based on collocated sonic using neural networks. *Measur Sci Tech* 27(9):095–901. <https://doi.org/10.1088/0957-0233/27/9/095901>
- Kit E, Cherkassky A, Sant T, Fernando HJS (2010) In situ calibration of hot-film probes using a collocated sonic anemometer: Implementation of a neural network. *J Atmosph Ocean Technol* 27(1):23–41. <https://doi.org/10.1175/2009JTECHA1320.1>
- Kit E, Hocut CM, Liberzon D, Fernando HJS (2017) Fine-scale turbulent bursts in stable atmospheric boundary layer in complex terrain. *J Fluid Mech* 833:745–772. <https://doi.org/10.1017/jfm.2017.717>
- Kit E, Barami E, Fernando HJS (2021) Structure functions in nocturnal atmospheric boundary layer turbulence. *Phys Rev Fluids* 6(084):605. <https://doi.org/10.1103/PhysRevFluids.6.084605>
- Lekakis I (1996) Calibration and signal interpretation for single and multiple hot-wire/hot-film probes. *Measur Sci Technol* 7(10):1313–1333. <https://doi.org/10.1088/0957-0233/7/10/004>
- Lekakis IC, Adrian RJ, Jones BG (1989) Measurement of velocity vectors with orthogonal and non-orthogonal triple-sensor probes. *Exp Fluids* 7(4):228–240. <https://doi.org/10.1007/BF00198002>
- Maciejewski PK, Moffat RJ (1994) Interpreting orthogonal triple-wire data from very high turbulence flows. *J Fluids Eng* 116(3):463–468. <https://doi.org/10.1115/1.2910299>
- Mammarella I, Dellwik E, Jensen NO (2008) Turbulence spectra, shear stress and turbulent kinetic energy budgets above two beech forest sites in Denmark. *Tellus B Chem Phys Meteorol* 60(2):179–187. <https://doi.org/10.1111/j.1600-0889.2007.00326.x>
- Metzger M, McKeon B, Holmes H (2007) The near-neutral atmospheric surface layer: turbulence and non-stationarity. *Philosoph Trans Royal Soc A Math Phys Eng Sci* 365(1852):859–876. <https://doi.org/10.1098/rsta.2006.1946>
- Meyers J, Meneveau C (2008) A functional form for the energy spectrum parametrizing bottleneck and intermittency effects. *Phys Fluids* 20(6):065–109. <https://doi.org/10.1063/1.2936312>
- Miller D, Lin J, Wang Y, Thistle H (1989) A triple hot-film and wind octant combination probe for turbulent air flow measurements in and near plant canopies. *Agricult Forest Meteorol* 44(3):353–368. [https://doi.org/10.1016/0168-1923\(89\)90028-2](https://doi.org/10.1016/0168-1923(89)90028-2)

- Pan Y, Chamecki M (2016) A scaling law for the shear-production range of second-order structure functions. *J Fluid Mech* 801:459–474. <https://doi.org/10.1017/jfm.2016.427>
- Patton EG, Horst TW, Sullivan PP, Lenschow DH, Oncley SP, Brown WOJ, Burns SP, Guenther AB, Held A, Karl T, Mayor SD, Rizzo LV, Spuler SM, Sun J, Turnipseed AA, Allwine EJ, Edburg SL, Lamb BK, Avissar R, Calhoun RJ, Kleissl J, Massman WJ, Paw UKT, Weil JC (2011) The canopy horizontal array turbulence study. *Bull Am Meteorol Soc* 92(5):593–611. <https://doi.org/10.1175/2010BAMS2614.1>
- Patton EG, Sullivan PP, Shaw RH, Finnigan JJ, Weil JC (2016) Atmospheric stability influences on coupled boundary layer and canopy turbulence. *J Atmosph Sci* 73(4):1621–1647. <https://doi.org/10.1175/JAS-D-15-0068.1>
- Peña A, Dellwik E, Mann J (2019) A method to assess the accuracy of sonic anemometer measurements. *Atmosph Measurment Tech* 12(1):237–252. <https://doi.org/10.5194/amt-12-237-2019>
- Podesta JJ, Forman MA, Smith CW, Elton DC, Malécot Y, Gagne Y (2009) Accurate estimation of third-order moments from turbulence measurements. *Nonlinear Process Geophys* 16(1):99–110. <https://doi.org/10.5194/npg-16-99-2009>
- Pope SB (2000) *Turbulent Flows*. Cambridge University Press
- Saddoughi SG, Veeravalli SV (1994) Local isotropy in turbulent boundary layers at high Reynolds number. *J Fluid Mech* 268:333–372. <https://doi.org/10.1017/S0022112094001370>
- Shapkalijevski M, Moene AF, Ouwersloot HG, Patton EG, de Arellano JVG (2016) Influence of canopy seasonal changes on turbulence parameterization within the roughness sublayer over an orchard canopy. *J Appl Meteorol Climatol* 55(6):1391–1407. <https://doi.org/10.1175/JAMC-D-15-0205.1>
- Shaw RH, Silversides RH, Thurtell GW (1974) Some observations of turbulence and turbulent transport within and above plant canopies. *Boundary-Layer Meteorol* 5(4):429–449. <https://doi.org/10.1007/BF00123490>
- Singha A, Sadr R (2013) In situ calibration of four-wire hot-wire probes for atmospheric measurement. *Exp Thermal Fluid Sci* 44:82–89. <https://doi.org/10.1016/j.expthermflusci.2012.05.016>
- Skelly BT, Miller DR, Meyer TH (2002) Triple-hot-film anemometer performance in cases-99 and a comparison with sonic anemometer measurements. *Boundary-Layer Meteorol* 105(2):275–304
- Sreenivasan KR, Antonia RA (1997) The phenomenology of small-scale turbulence. *Annu Rev Fluid Mech* 29(1):435–472. <https://doi.org/10.1146/annurev.fluid.29.1.435>
- Sreenivasan KR, Dhruva B (1998) Is there scaling in high-reynolds-number turbulence? *Prog Theoret Phys Suppl* 130:103–120. <https://doi.org/10.1143/PTPS.130.103>
- Su HB, Schmid HP, Grimmond CSB, Vogel CS, Oliphant AJ (2004) Spectral characteristics and correction of long-term eddy-covariance measurements over two mixed hardwood forests in non-flat terrain. *Boundary-Layer Meteorol* 110(2):213–253
- Tsuji Y (2004) Intermittency effect on energy spectrum in high-Reynolds number turbulence. *Phys Fluids* 16(5):L43–L46. <https://doi.org/10.1063/1.1689931>
- Wyngaard JC, Clifford SF (1977) Taylor's hypothesis and high-frequency turbulence spectra. *J Atmosph Sci* 34(6):922–929. [https://doi.org/10.1175/1520-0469\(1977\)034<0922:THAHTS>2.0.CO;2](https://doi.org/10.1175/1520-0469(1977)034<0922:THAHTS>2.0.CO;2)

Publisher's Note Springer Nature remains neutral with regard to jurisdictional claims in published maps and institutional affiliations.

Springer Nature or its licensor (e.g. a society or other partner) holds exclusive rights to this article under a publishing agreement with the author(s) or other rightsholder(s); author self-archiving of the accepted manuscript version of this article is solely governed by the terms of such publishing agreement and applicable law.